Elucidating the origin of long-range ferromagnetic order in Fe_3GeTe_2 by low-energy magnon excitation studies

B. G. Beier,[1] E. S. Beier,[1] J. Arneth,[1] E. Brücher,[2] R. K. Kremer,[2] and R. Klingeler[1,*]
[1]*Kirchhoff Institute for Physics, Heidelberg University, INF 227, D-69120 Heidelberg, Germany*
[2]*Max Planck Institute for Solid State Research, Heisenbergstraße 1, D-70569 Stuttgart, Germany*

(Received 19 July 2025; accepted 3 November 2025; published 8 December 2025)

We report a detailed high-field/high-frequency ferromagnetic resonance (HF-FMR) study of low-energy magnon excitations in the van der Waals ferromagnet $Fe_{2.92(1)}Ge_{1.02(3)}Te_2$. At 2 K, the field dependence of the magnon branches is well described by a semiclassical domain-based model, from which we extract key microscopic parameters including the anisotropy gap $\Delta = 170(4)$ GHz, the anisotropy field $B_A = 5.85(8)$ T, and the effective g-factor $g_{ab} = g_c = 2.07(4)$. Furthermore the uniaxial anisotropy constant is determined to be $K = 10.50(23) \times 10^6$ erg/cm^3. Anisotropic short-range magnetic order persists above T_C up to approximately 270 K, as evidenced by a finite anisotropy gap and anisotropic shifts in the ferromagnetic resonance (FMR) resonance fields. Both results clearly show the presence of anisotropic local magnetic fields well above T_C. Our findings underscore the crucial role of magnetocrystalline anisotropy in driving long-range magnetic order in Fe_3GeTe_2.

DOI: 10.1103/zf74-j18j

I. INTRODUCTION

Reducing one dimension of a material below characteristic lengthscales to achieve two-dimensional (2D) systems can yield spectacular novel properties as evidenced among many other examples by the quantum Hall effect, Dirac fermions in graphene, superconductivity in cuprates, or the appearance of topological phases [1–4]. The pronounced strength of thermal as well as of quantum fluctuations in systems with reduced dimensionality, in particular, challenges long-range (magnetic) ordering phenomena by establishing quantum ground states and critical phenomena [5–11] and hence opens a wide field for fundamental research. It also offers new routes for technological applications. The recent advances in the research field of 2D van der Waals (vdW) materials illustrate these prospects as progress in our understanding of low-dimensional materials is accompanied by exploiting these properties in actual devices (see, e.g., Refs. [12–16]). In this respect, the existence of long-range ferromagnetic (FM) order is particularly important for magnetic devices. Since, in the strict 2D Heisenberg case, long-range magnetic order does not evolve for any short-range in-plane magnetic exchange [5], magnetic anisotropy is a crucial ingredient for establishing ferromagnetism and to drive it beyond room temperature [17,18]. While several semiconducting FM 2D vdW materials are known (e.g., CrI_3, $CrGeTe_3$, $CrSiTe_3$, $CrBr_3$, $(Cr,Fe)Cl_3$, see Refs. [19–25] and for a review Ref. [26]), the family of Fe_nGeTe_2 ($n \simeq 3, 4, 5$) materials offers the rare case of metallic 2D ferromagnets [27–29] with FM ordering temperatures T_C approaching or even exceeding room temperature [17,30] (see also Table I). From this family, Fe_3GeTe_2 offers great potential for application in magnetic heterostructures and spintronics which is further boosted by its good air stability [27]. Recent studies exploiting the low-dimensional metallic nature of Fe_3GeTe_2 have found, e.g., a large anomalous Hall effect [13], evidence of Kondo lattice physics and heavy-fermion states [31], skyrmions [32], and a moderate magnetocaloric effect [33].

Fe_3GeTe_2 features iron germanium layers which are sandwiched by tellurium atoms and only weakly bound via vdW bonds [27] (see Fig. 1). The projection of the iron atoms to the *ab* plane shows a hexagonal arrangement with germanium atoms in the center of each hexagon as shown in Fig. 1(b). There are two differently coordinated iron sites Fe1 and Fe2 which are positioned at different heights along the *c* axis in each hexagon. Even for samples prepared under stoichiometric conditions, the Fe2 site is not fully occupied [35].

In comparison with other FM vdW materials, Fe_3GeTe_2 exhibits high uniaxial magnetocrystalline anisotropy (see Table I) and its magnetic behavior can be tuned through a variation of iron deficiency [36], the number of layers [37], or by strain tuning [38] (see also the review in Ref. [39]). Despite extensive previous research, the microscopic origin of long-range FM order in Fe_3GeTe_2 still remains an open question. Prior studies focusing on whether the FM ordering arises from itinerant or localized magnetic moments lead to contradictory conclusions [31,40,41].

In this work, we investigate low-energy magnon excitations in Fe_3GeTe_2 using high-field/high-frequency ferromagnetic resonance (HF-FMR). The field dependence of the magnon branches at 2 K yields the size of the anisotropy gap, the anisotropy field, and the effective g-factor of Fe_3GeTe_2, which are also used to determine the uniaxial anisotropy constant. Furthermore, from HF-FMR measurements at various temperatures we find that long-range order develops from anisotropic

*Contact author: klingeler@kip.uni-heidelberg.de

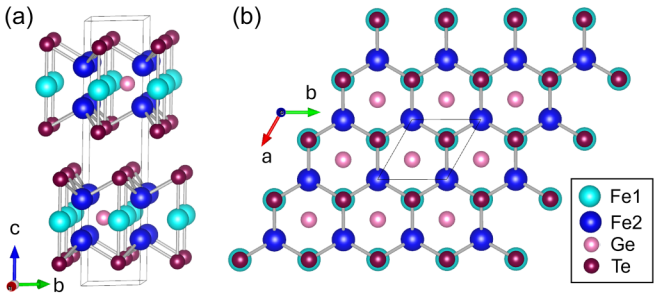

FIG. 1. Crystal structure of Fe_3GeTe_2 [27]: (a) Unit cell and (b) top view of *ab* plane. The figures were generated with VESTA [34].

short-range order which is quasistatic on the GHz timescale in a wide temperature regime above T_C. Our findings underscore the crucial role of magnetocrystalline anisotropy and elucidate the origin of long-range magnetic order in Fe_3GeTe_2.

II. EXPERIMENT

High-field/high-frequency electron spin resonance (HF-ESR) measurements were performed in the frequency range 40 GHz $\leqslant f \leqslant$ 850 GHz in transmission mode and Faraday configuration. The generation and detection of the microwave radiation was facilitated by means of a millimeter-wave vector network analyzer from AB Millimetre [42]. The measurements were performed in a magnetocryostat system (Oxford) equipped with a 16 T superconducting coil and a variable temperature insert (VTI) operating in the range 1.7 K $\leqslant T \leqslant$ 300 K [43]. The measurements were performed on an approximately rectangularly shaped thin single crystal of dimensions $2.8 \times 2.7 \times 0.3$ mm^3 fixed in a brass ring (see also the Supplemental Material (SM) [44]). The sample originates from the same batch as in Ref. [35], where the atomic site occupancy was determined to be $Fe_{2.92(1)}Ge_{1.02(3)}Te_2$, implying an identical composition for our sample. The static magnetization was measured in a Quantum Design MPMS3 superconducting quantum interference device (SQUID) magnetometer operating with the magnetic field applied parallel to the crystallographic *c* axis of the material. Our data (see $M(T, B = 1\ \text{T})$ in Fig. S2 in the SM [44]) show identical behavior as reported in Ref. [35] where, from modified Arrot-Belov plots, $T_C = 217$ K was determined.

III. RESULTS

A. Ferromagnetic resonance modes at $T = 2$ K

First, we report the magnetic field dependence of the ferromagnetic magnon modes in Fe_3GeTe_2 at low temperature. The ferromagnetic resonance (FMR) spectra were obtained at $T = 2$ K, i.e., well below the ferromagnetic ordering temperature, and show several resonance features associated with magnon excitations. The corresponding spectra for $B||c$ axis and $B||ab$ plane are shown in Fig. 2. The resonance features are marked by colored symbols and can be clearly identified in the spectra as the amplitude and the phase of the signal was measured in both up- and down-sweeps of the field. For $B||c$ axis a single resonance branch ν_3 is detected. In contrast, there are two distinct resonance features ν_1 and ν_2 in the spectra obtained for $B||ab$ plane, the former being observed only up to $f = 148.2$ GHz. There are a few further resonance features (grey symbols in Figs. 2 and 3) which stem from the sample holder including kapton sealing tape (e.g., at approx. 2 T for $f = 54.5$ GHz and $f = 60.2$ GHz) or cannot be attributed to any distinct resonance branch. The assignment of the extra features to the sample holder was confirmed by empty sample holder measurements. The corresponding resonance

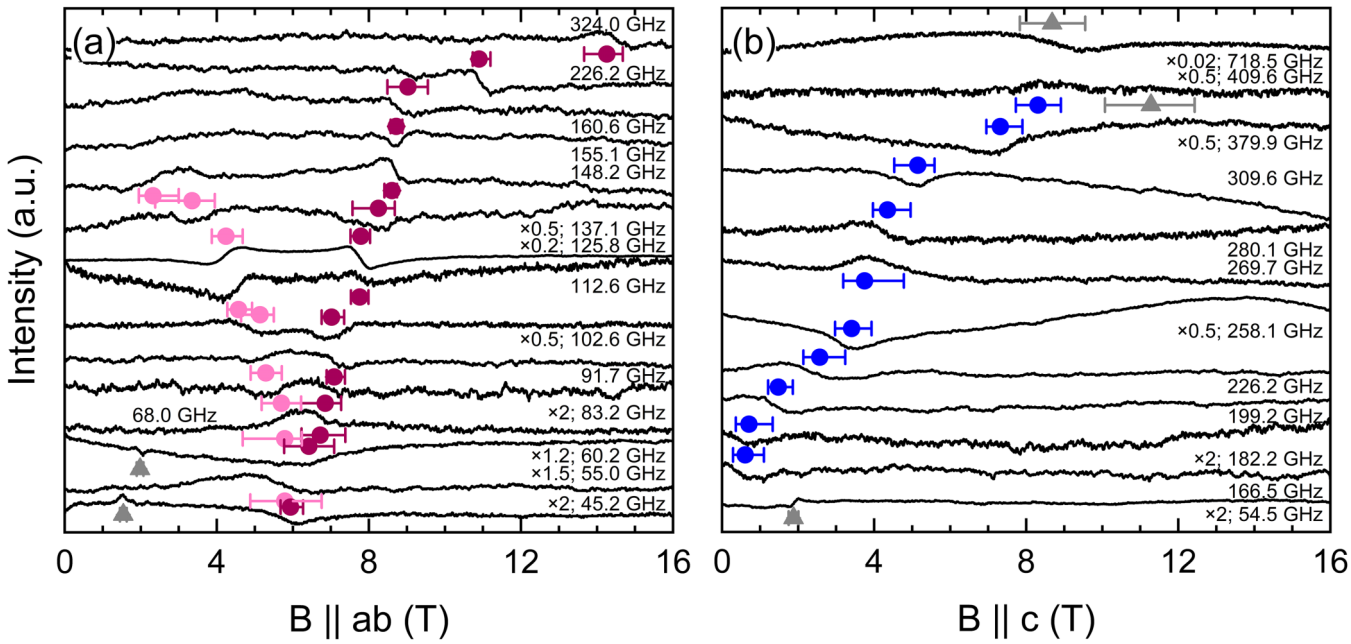

FIG. 2. HF-ESR spectra at selected frequencies obtained at $T = 2$ K for (a) $B||ab$ plane (ν_1, ν_2) and (b) $B||c$ axis (ν_3). Colored symbols mark the positions of the resonance features. Some spectra were corrected for a linear or quadratic background.

fields are summarized in the resonance-frequency-magnetic-field diagram (fB diagram) in Fig. 3. The fB diagram shows the three distinct resonance branches mentioned above which main qualitative features are as follows: (1) Two modes (ν_1, ν_3) demonstrate a zero-field excitation gap of about $\tilde{\Delta} \simeq$ 170 GHz. (2) The in-plane modes ν_1, ν_2 soften at about $\simeq 6\,\mathrm{T}$ with distinct (ν_1) or modest (ν_2) bending. (3) The high-frequency behaviors of ν_2 and ν_3 are quasilinear with approximately the same slopes.

To model the field dependence of the three distinct resonance branches in detail, the domain-based model for FMR modes in materials with the easy-axis parallel to the crystallographic c axis and in Faraday configuration is applied. The model predicts three FMR modes—i.e., the solutions of the Larmor equations obtained by using the Smit-Beljers approach—with the following field dependencies of the resonance frequencies [45,46]: For $B_{\mathrm{res}}||ab$:

$$\left(\frac{\nu}{\gamma_{\mathrm{ab}}}\right)^2 = \begin{cases} \left(\frac{\nu_1}{\gamma_{\mathrm{ab}}}\right)^2 = (B_{\mathrm{A}} + N_{\mathrm{x}}M_{\mathrm{s}})(B_{\mathrm{A}} + M_{\mathrm{s}}\sin^2\alpha) - \dfrac{(B_{\mathrm{A}} + M_{\mathrm{s}}\sin^2\alpha - N_{\mathrm{z}}M_{\mathrm{s}})(B_{\mathrm{A}} + N_{\mathrm{x}}M_{\mathrm{s}})}{(B_{\mathrm{A}} + N_{\mathrm{y}}M_{\mathrm{s}})^2}B_{\mathrm{res}}^2, & B_{\mathrm{res}} \leqslant B_{\mathrm{sat}} \quad (1) \\ \left(\frac{\nu_2}{\gamma_{\mathrm{ab}}}\right)^2 = (B_{\mathrm{res}} - (B_{\mathrm{A}} - (N_{\mathrm{z}} - N_{\mathrm{y}})M_{\mathrm{s}}))(B_{\mathrm{res}} - (N_{\mathrm{y}} - N_{\mathrm{x}})M_{\mathrm{s}}), & B_{\mathrm{res}} \geqslant B_{\mathrm{sat}}. \quad (2) \end{cases}$$

For $B_{\mathrm{res}}||c$:

$$\frac{\nu_3}{\gamma_{\mathrm{c}}} = B_{\mathrm{res}} + B_{\mathrm{A}} - N_{\mathrm{z}}M_{\mathrm{s}}. \quad (3)$$

Here, α corresponds to the angle a certain magnetic domain wall encloses with the external applied magnetic field; B_{A} is the anisotropy field; M_{s} the saturation magnetization; N_{x}, N_{y}, and N_{z} are the demagnetization factors; and $\gamma_{\mathrm{ab/c}}$ are the gyromagnetic ratios for $B||ab/B||c$ in units of GHz/T. The gyromagnetic ratio is then given by $(\mu_{\mathrm{B}}/h) \times g_{\mathrm{ab/c}}$, where $g_{\mathrm{ab/c}}$ are the effective g-factors, related to the slope of the resonance branches in the fB-diagram for the respective field directions, μ_{B} is the Bohr magneton and h is the Planck constant. At high magnetic fields $B \geqslant B_{\mathrm{sat}} = B_{\mathrm{A}} + N_{\mathrm{y}}M_{\mathrm{s}}$, the system adopts the fully polarized spin configuration which is well described by a single domain model and the respective resonance branch ν_2 [Eq. (2)].

The demagnetization factors were determined to be $N_{\mathrm{x}} = 0.097(4)$, $N_{\mathrm{y}} = 0.099(5)$, $N_{\mathrm{z}} = 0.804(9)$ by assuming a perfect rectangularly shaped crystal with the above-mentioned dimensions using the formulas from Ref. [47]. To account for potential deviations from these values, e.g., due to imperfect rectangular shape or the finite penetration depth in the metallic sample, fits of the domain-based model were also performed with the demagnetization factors as free parameters. The determined values for B_{A}, α, and $\gamma_{\mathrm{ab/c}}$ did not change significantly. Therefore, to determine B_{A}, α, and $\gamma_{\mathrm{ab/c}}$ from the experimental data, the above-mentioned values for $N_{\mathrm{x}}-N_{\mathrm{z}}$ calculated for a perfect rectangularly shaped crystal were used as an approximation for the demagnetization factors of the nonperfectly shaped crystal measured in this work. The saturation magnetization was determined from the isothermal magnetization data (see Fig. S2 in the SM [44]) to $M_{\mathrm{S}} = 4.36(7)\,\mu_{\mathrm{B}}/\mathrm{f.u.}$.

As illustrated in Fig. 3, the observed resonance branches $\nu_1-\nu_3$ are well described by Eqs. (1)–(3). The experimental data of all branches were simultaneously fitted. The three lowest-lying resonance features ($f = 45.2\,\mathrm{GHz}$, $55.0\,\mathrm{GHz}$, $60.2\,\mathrm{GHz}$) were assigned to the resonance branches ν_1 and ν_2 such that the deviation of the fit from the data is minimized. The best fit to the data yields $B_{\mathrm{A}} = 5.85(8)\,\mathrm{T}$, $g_{\mathrm{ab}} = g_{\mathrm{c}} = 2.07(4)$, and $\alpha = 0(11)^\circ$.

The domain-based model applied here assumes the presence of magnetic domains with different orientations of the magnetization within neighboring domains. For comparison, we fitted the field dependence of the three magnon branches at 2 K also by a single domain model where $\tilde{\nu_1}$ is described by Eq. S1 in the SM [44]. This single-domain model, however, yields an unsatisfactory description of the experimental data. In particular, it fails to describe the resonance branch ν_1 since it does not capture the experimentally observed pronounced bending which is reproduced well in the domain-based model (see Fig. S5 in the SM [44]). Our experimental data hence reveals the presence of domains in Fe_3GeTe_2.

The experimental data presented in Fig. 3 clearly show the presence of a zero-field excitation gap $\tilde{\Delta}$ which is attributed to magnetic anisotropy. While its approximate value

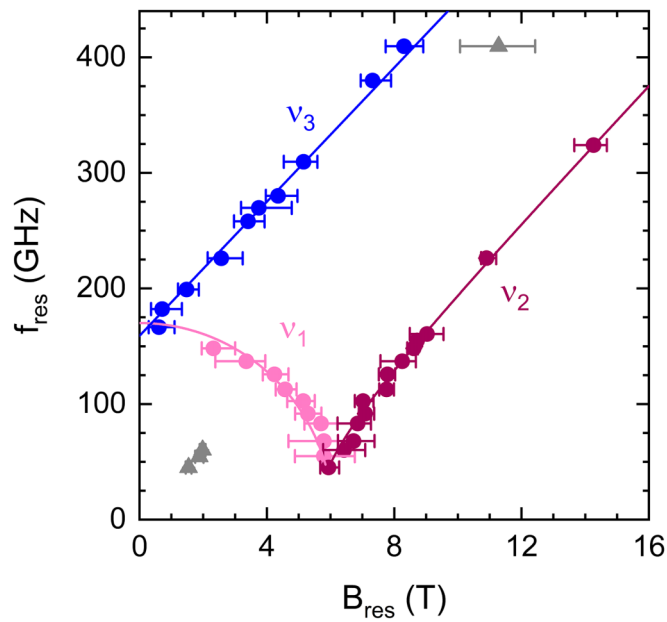

FIG. 3. Resonance-frequency–magnetic-field diagram of Fe_3GeTe_2 at 2 K. The resonance branches for $B||ab$ plane ($B||c$) are labeled ν_1/ν_2 (ν_3). Solid lines are fits to the data using the domain-based model described in the text.

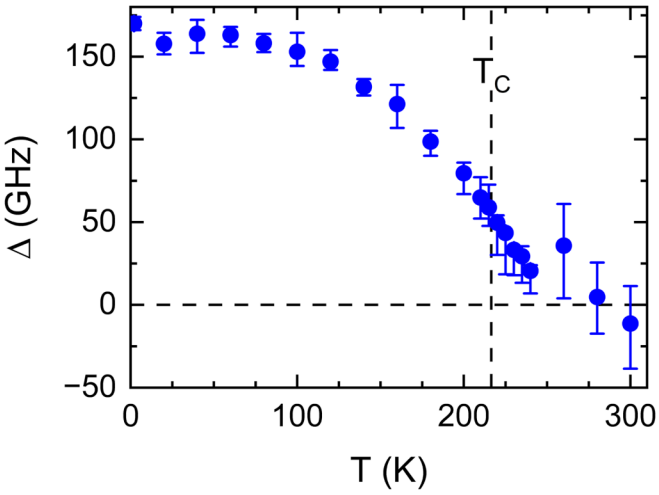

FIG. 4. Temperature dependence of the anisotropy gap Δ as described in the text. The vertical dashed line marks T_C.

can be directly read-off in the fB-diagram, its more precise determination is feasible by exploiting the fit results of the domain-based model to the resonance branches $\nu_1-\nu_3$. This procedure yields $\Delta = \gamma B_A = 170(4)$ GHz for the anisotropy gap at $T = 2$ K. Δ is associated with the f-axis intersection (i.e., $\tilde{\Delta}$) of the resonance branches ν_1 and ν_3 of the domain-based model. Calculating this intersection, e.g., for ν_3 by setting $B_{res} = 0$ in Eq. (3) yields $\tilde{\Delta} = \gamma_c B_A - \gamma_c N_z M_S$ and therefore the relation $\Delta = \gamma_c B_A = \tilde{\Delta} + \gamma_c N_z M_S$.

B. Temperature dependence of the FMR modes and quasistatic magnetic fields well above T_C

The effect of increasing the temperature on the dynamic magnetic response is studied by means of the temperature evolution of the anisotropy gap and of the effective g_c factor. To this end we recorded fB-diagrams for $B||c$ axis for temperatures between 2 K and 300 K (see Fig. S4 in the SM

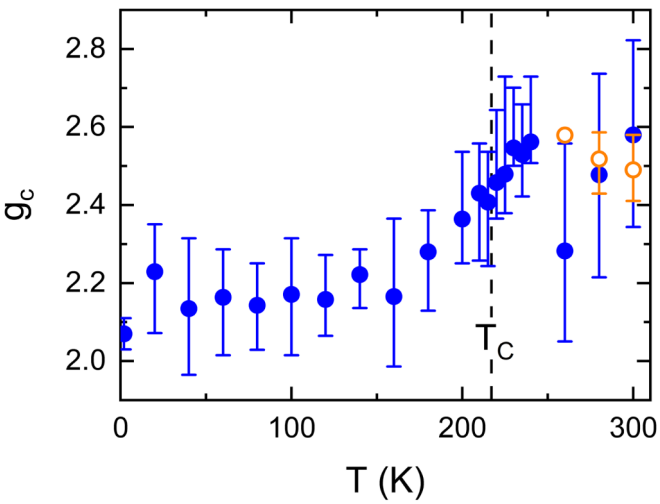

FIG. 5. Temperature dependence of the effective g_c-factor determined as described in the text. Open (orange) data points correspond to fits with $\tilde{\Delta}$ fixed to zero. The vertical dashed line marks T_C.

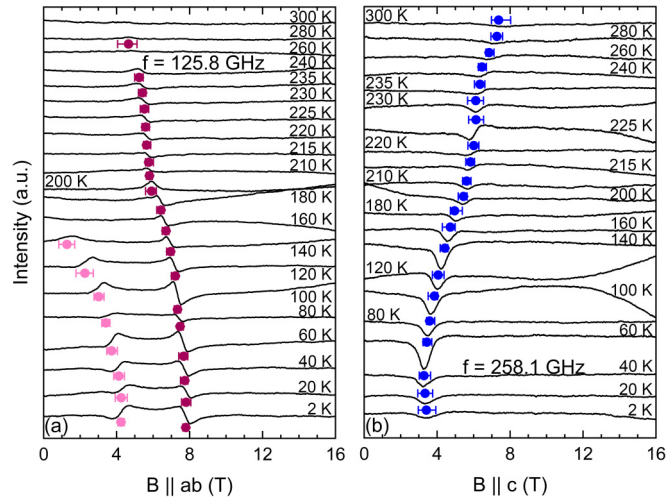

FIG. 6. HF-ESR spectra at various temperatures at fixed frequencies for (a) $B||ab$ plane (at $f = 125.8$ GHz) and (b) $B||c$ axis (at $f = 258.1$ GHz). Colored symbols mark the positions of the resonance features. Where needed the spectra were corrected for a linear or quadratic background.

[44]). For all temperatures, the resonance frequencies linearly depend on the magnetic field. The slope of the resonance branches enables us to determine the effective g-factors, g_c, while their linear extrapolation to zero magnetic field yields the associated excitation gap $\tilde{\Delta}$. The obtained temperature dependencies of the demagnetization-corrected anisotropy gap Δ and g_c are visualized in Figs. 4 and 5.

The zero-field anisotropy gap Δ is rather constant at low temperatures but significantly decreases upon heating (see Fig. 4). Notably, Δ is still finite at T_C where it assumes the value of ≈65 GHz, i.e., ≈38 % of its low-temperature value. We observe a finite gap above T_C which only vanishes for $T \gtrsim T_\Delta \simeq 270$ K (≈1.25T_C). Our data, in particular, do not indicate any distinct anomaly at T_C, which implies that on the GHz timescale the (static) long-range ordering temperature is not decisive. This observation is directly visible in our experimentally observed fB diagrams (see Fig. S4 in the SM [44]) from which the presence and size of the gap can be directly read off while the demagnetization corrections ($\gamma_c N_z M_s$) are only small. The saturation magnetization M_s at each temperature used for the demagnetization correction was approximated by the magnetization measured for $B||c$ at $B = 1\,\mathrm{T} \gg B_{sat,c}$ (see Fig. S2 in the SM [44]), where $B_{sat,c}$ denotes the saturation field at 2 K for $B||c$. Consequently, the size of the correction decreases with increasing temperature and amounts to approximately 5 GHz at T_C, which is a magnitude smaller than $\Delta(T = T_C)$.

Concomitantly, the effective g_c-factor derived from the data in Fig. S4 in the SM [44] remains constant at low temperatures, increases above ∼160 K, and again assumes an approximately constant value of $g_c \simeq 2.55$ for $T \gtrsim T_C$. To further reduce the number of fitting parameters, we exploit that, for $T \gtrsim 260$ K, the excitation gap $\tilde{\Delta}$ assumes values close to 0 GHz (see Fig. 4). We conclude that it vanishes in this temperature regime as expected for sufficiently high temperatures. We hence have performed linear fits based on Eq. (3) with $\tilde{\Delta}$ fixed to zero to extract g_c above 260 K. The

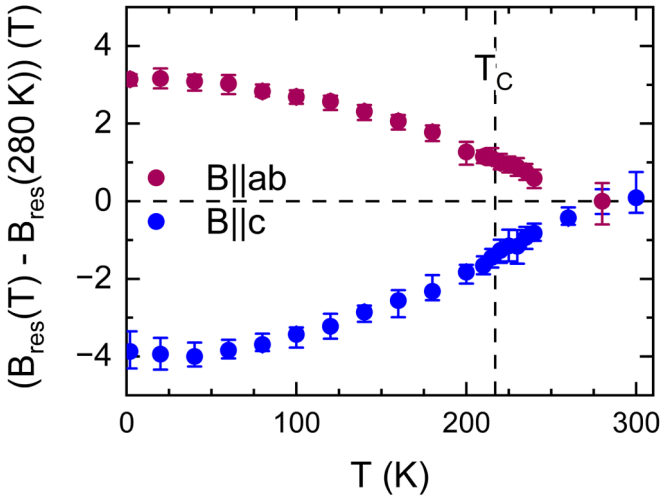

FIG. 7. Temperature dependence of the shift of the resonance fields at $f = 125.8\,\mathrm{GHz}$ ($B||ab$ plane) and $f = 258.1\,\mathrm{GHz}$ ($B||c$ axis) from its value at 280 K. The vertical dashed line marks T_C.

resulting g_c values exhibit much smaller error bars and suggest that g_c slightly decreases with increasing temperature above T_C (see Fig. 5). A comparable qualitative behavior of g_c with a more pronounced increase of g_c towards T_C was observed in the literature for CrI_3 [48], $CrSiTe_3$ [45], and $CrGeTe_3$ [30,45].

The observation of a finite anisotropy gap well above T_C indicates the presence of quasistatic magnetic order on the timescale of the experiment, i.e., in the 10^2-GHz regime, in this temperature range. To further prove this scenario, we studied the evolution of the actual local fields with temperature by measuring the resonance fields at selected frequencies. These measurements were performed for $B||c$ axis and $B||ab$ plane at $f = 258.1\,\mathrm{GHz}$ and $f = 125.8\,\mathrm{GHz}$, respectively, in the temperature regime $2\,\mathrm{K} \leqslant T \leqslant 300\,\mathrm{K}$. The recorded spectra are shown in Fig. 6. For $B||ab$ plane, we observe two resonance features which both shift to lower magnetic fields with increasing temperature. For $B||c$ axis, in contrast, the resonance shifts to higher magnetic fields upon heating. The shifting of the resonance field positions continues above T_C.

The resonance fields obtained from the measurements shown in Fig. 6 were used to determine the shift of the resonance fields with respect to the resonance field at the highest measured temperature where the resonances for $B||ab$ plane and $B||c$ axis are both still visible (280 K; see Fig. 6). This shift is visualized in Fig. 7. $|B_{res}(T) - B_{res}(280\,\mathrm{K})|$ decreases with increasing temperature for both directions of the external applied magnetic field and vanishes only well above T_C. It should be again noted here that the shift of the resonance position is anisotropic up to $\simeq 270\,\mathrm{K}$, as the resonance fields for $B||ab$ plane and $B||c$ axis shift in an opposite manner.

Since the resonance field positions probe the actual local fields, the observed shifts clearly prove the monotonous increase of quasistatic anisotropic fields upon cooling. Both the temperature dependence of Δ and of the local fields hence imply anisotropic short-range magnetic order up to at least $270\,\mathrm{K} \gg T_C$. We again emphasize the absence of any discontinuity at T_C which shows that, at the timescale of our experiments, the evolution of true long-range magnetic order does not yield any significant changes of the local magnetic properties.

C. Discussion

1. Anisotropy gap Δ at $T = 2$ K

At 2 K, the field dependence of the three observed magnon branches is well captured by the domain-based model as shown in Fig. 3. The saturation field $B_{sat} = B_A + N_y M_S = 5.89(8)\,\mathrm{T}$ for $B||ab$ obtained from the simultaneous fit for $B||ab$ and $B||c$ is in good agreement with the reported magnetization data [49]. Our data in particular enable us to precisely determine the anisotropy gap of the magnon branches which, at $T = 2\,\mathrm{K}$ amounts to $\Delta = 170(4)\,\mathrm{GHz}$. The uniaxial anisotropy constant can be calculated from the fit parameters by $K = M_S\Delta/(2\gamma)$, yielding $K = 10.50(23) \times 10^6\,\mathrm{erg/cm^3}$ at $T = 2\,\mathrm{K}$.

The comparison of the excitation gap determined here with reported data from inelastic neutron scattering (INS) on Fe_3GeTe_2 in Table II illustrates that Fe site occupancy is a crucial parameter not only for Δ but also for T_C. The Fe site occupancy is supposed to govern T_C by altering the density of states and the lattice constants and thereby tuning the magnetic interaction and anisotropy energies [50,51]. In the 2D limit of a Heisenberg ferromagnet, the relation between T_C, the exchange interaction J and the uniaxial anisotropy constant K—which is proportional to the anisotropy gap by $K = \Delta M_S/(2\gamma)$—is given by [52]

$$T_C \propto \frac{J}{\ln(\pi^2 J/K)}. \tag{4}$$

Considering the recent analysis [53] of the Q^2 behavior of the spin waves in $Fe_{2.72}GeTe_2$, the data imply that the significantly reduced ordering temperature of only $\sim$160 K compared to the two samples with smaller iron deficiency is directly associated with the smaller anisotropy gap. The anisotropy gap obtained from INS [54] for a sample with a similar iron deficiency and similar T_C as used in this work does not deviate significantly from the one determined in this work by HF-FMR. However, considering the error bars, HF-FMR allows for a much more precise determination of the anisotropy gap as compared to the INS reports [50,53,54].

2. Domain structure

In the literature the domain wall configuration of the *ab* plane was studied frequently [37,55–59]. Depending on the thickness of the sample, the temperature, the cooling procedure and the applied magnetic field stripe domains, labyrinth domains, wavy-stripes with bubble domains, circular domains with double-domain structure, branching features, and bubble domains were observed in the *ab* plane of Fe_3GeTe_2 [37,55–59]. In all of the mentioned studies, where a magnetic field was applied, the field was applied parallel to the *c* axis. Our FMR experiments in contrast provide information on the domain wall configuration of the sample surface with normal vector perpendicular to the crystallographic *c* axis and magnetic field applied parallel to the *ab* plane: The parameter $\alpha = 0(11)^\circ$ present in Eq. (1) denotes the angle between the

TABLE I. Microscopic anisotropy-related parameters of FM vdW materials determined by FMR. Listed parameters are the following: Anisotropy type [uniaxial (u) or planar (p)], critical temperature T_C, relation $\frac{T_\Delta}{T_C}$ [unknown (uk) refers to samples were FMR was not measured at $T > T_C$], anisotropy gap Δ, anisotropy field B_A, and anisotropy constant K.

	u/p	T_C (K)	T_Δ/T_C	Δ (GHz)	B_A (T)	K (erg/cm^3)	Ref.
Fe_3GeTe_2	u	217	1.25	170(4) @2 K	5.85(8) @2 K	$10.50(23) \times 10^6$ @2 K	This work
Fe_4GeTe_2	u[a]	≈270	>1.11	≈30.6 ($B\|\|c$) @3 K[b] ≈15 ($B\|\|ab$) @ 3 K[b]	≈1.07 ($B\|\|c$) @ 3 K[b] ≈0.5 ($B\|\|ab$) @ 3 K[b]	≈2.9×10^6 ($B\|\|c$) @ 3 K ≈1.4×10^6 ($B\|\|ab$) @ 3 K	[60]
Fe_5GeTe_2	p	332	uk	≈6.4 @ 100 K[c]	≈0.22 @ 100 K[d]	4.81×10^5 @ 100 K	[17]
$CrBr_3$	u	37	uk	≈18 @ 10 K[d]	≈0.56 @ 10 K	7.2×10^5 @ 1 K	[61]
CrI_3	u	61	≈1.3	80(1) @ 2 K	2.8(1) @ 2 K	$2.9(9) \times 10^6$ @ 2 K[e]	[48]
	u	68	uk	≈42 @ 10 K[d]	≈2.7 @ 10 K	≈2.9×10^6 @ 10 K	[61]
	u	68	uk	82.9 @ 1.5 K[f]	2.86 @ 1.5 K	3.1×10^6 @ 1.5 K	[62]
$CrSiTe_3$	u	34	≈1	≈33 @ 10 K[d]	≈1.14 @ 10 K[d,g]	≈5.4×10^5 @ 10 K[d,h]	[63]
$CrGeTe_3$		≈68	≈1	≈16.5 @ 10 K[d]	≈0.58 @ 10 K[d,i]		[63] (SM)
	u	64.7(5)	uk	≈9 @ 2 K[d]	≈0.3 @ 2 K[d]	4.0×10^5 @ 2 K	[30]
	u	66(1)	1.5	≈7 @ 4 K[d]	≈0.25 @ 4 K[d]	$4.8(2) \times 10^5$ @ 4 K	[64]
	u	≈61	uk		≈0.49 @ 5 K	≈3.65×10^5 @ 5 K	[65]
	u	67.9	1	≈6 @ 40 K[d]	≈0.22 @ 40 K[d]	≈1.9×10^5 @ 40 K[d,j]	[66]

[a]The intrinsic magnetic anisotropy is of easy-axis type [60]. A more complex behavior at low temperatures is reported and yield distinct values for Δ and B_A for different magnetic field directions [60].
[b]Obtained as $\Delta = \gamma B_A = 2\gamma K/M_S$ with $K \approx 2.9 \times 10^6$ erg/cm^3 ($B||c$), $K \approx 1.4 \times 10^6$ erg/cm^3 ($B||ab$), $g_c = 2.045(32)$, $g_{ab} = 2.073(15)$, and $M_S \approx 539.19$ erg/(cm^3 G) from Ref. [60].
[c]Obtained as $\Delta = \gamma B_A$ with $B_A \approx 0.22$ T[d], $g \approx 2.1$ from Ref. [17].
[d]No demagnetization correction was applied.
[e]Obtained as $K = B_A M_S/2$ with $B_A = 2.81(10)$ T and $M_S = 3.0(10)\,\mu_B$/f.u. from Ref. [48].
[f]Obtained as $\Delta = \gamma B_A$ with $B_A = 2.86$ T and $g = 2.07$ from Ref. [62].
[g]Obtained as $\Delta = \gamma B_A$ with $\Delta \approx 33$ GHz[d] and $g \approx 2.07$ from Ref. [63].
[h]Obtained as $K = B_A M_S/2$ with $B_A \approx 1.14$ T, $M_S \approx 2.8\,\mu_B$/f.u. [63] and No. of f.u./unit cell = 3, $V_{\text{unitcell}} = 0.8301(1)$ pm^3 [67].
[i]Obtained as $\Delta = \gamma B_A$ with $\Delta \approx 16.5$ GHz[d] and $g \approx 2.03$ from Ref. [63] (SM).
[j]Obtained as $K = B_A M_S/2$ with $B_A \approx 0.22$ T[d] and $M_S \approx 30$ erg/(G g) [66].

domain walls and the applied magnetic field direction. In this respect we, however, note the rather high conductivity of Fe_3GeTe_2 [13,27] implying a penetration depth smaller than about 10 nm[1] so that the applied microwave radiation cannot fully penetrate the sample which exhibits a thickness of 200 μm. Our experiment hence probes small portions and edges of the sample and its ferromagnetic domain structure, i.e., the surface of the sample. This is confirmed by observing the HF-FMR signal also when the sample is covered by aluminium foil to exclude transmission through the bulk (see Fig. S3 in the SM [44]). For the probed volume, our observation of $\alpha \simeq 0^\circ$ indicates that at the sample surface with normal vector perpendicular to the crystallographic c axis the distribution of domain wall orientations is centered parallel to the applied magnetic field direction. This suggests a predominantly stripe domain arrangement at the surface, as illustrated in Fig. S6 in the SM [44].

For the ab plane, it has been shown that the stripe-like domains of the labyrinthine domain structures in Fe_3GeTe_2 for higher temperatures and zero magnetic field tend to align preferentially perpendicular to the sample surface [55], which is also the case for the surface measured in the current work at low temperatures and applied magnetic field (see Fig. S6 in the SM [44]). In CrI_3, in contrast to Fe_3GeTe_2, the domain structure is characterized by two main orientations of the domain walls: perpendicular and parallel to the applied magnetic field, where the latter is the predominant one [48].

3. *Anisotropic short-range order above T_C*

Short-range magnetic correlations in Fe_3GeTe_2 above T_C are expected due to its low-dimensional nature but experimental evidence reported in the literature is either ambiguous or appears in micropatterned material: In the neutron scattering data reported in Ref. [50], a characteristic ring feature in the hk plane is well visible above T_C, which might originate from short-range magnetic order. However, it was stated that phonon scattering could also lead to this observation [50]. The authors of Ref. [55] reported a non-paramagnetic state above T_C in micropatterned Fe_3GeTe_2 where magnetic domains were observed up to room temperature [55].

The experimental FMR data presented above clearly confirm the presence of short-range magnetic order in Fe_3GeTe_2 well above T_C by detecting anisotropic local magnetic fields and a finite anisotropy gap at the 100 GHz timescale. From our

[1]The penetration depth of the electromagnetic wave into a conductor is given by $\delta \approx \sqrt{2/\omega\mu\sigma}$, where $\omega \approx 1 \times 10^{11} - 1 \times 10^{12}$ 1/s is the angular frequency of the used microwave, $\mu = 1 + \chi$ the permeability of Fe_3GeTe_2, and $\sigma \approx 1 \times 10^5 - 1 \times 10^6$ Ωm is the conductivity of Fe_3GeTe_2 [13,27]. As the magnetic susceptibility $\chi > 0$ for FMs, the largest possible penetration depth is in the order of 10 nm.

data, we conclude the existence of three distinct temperature regimes:

(1) For $T \gtrsim T_\Delta$ ($T_\Delta \sim 270$ K), we find vanishing of Δ and there are no quasistatic anisotropic magnetic fields. However, at $T \simeq 300$ K we still observe a rather large g factor of $g_c \simeq 2.5$ and different resonance fields for $B||ab$ plane and $B||c$ axis. This suggests that at 300 K a pure paramagnetic (PM) regime is not yet reached. This agrees with indications for a non-PM state in Fe_3GeTe_2 extending up to room temperature reported in the literature [50,55]. (2) For $T_C \lesssim T \lesssim T_\Delta$ we observe clear evidence of anisotropic short-range magnetic order, as Δ is finite and there are anisotropic shifts of the resonance fields. In addition to this, a plateau in g_c is obtained in this temperature region. (3) The development of long-range magnetic order in Fe_3GeTe_2 is not associated with clear anomalies in the FMR spectra as we do not observe any anomalies in the temperature evolution of Δ and g_c at T_C. Specifically, while Δ assumes finite values below ~270 K and smoothly increases upon cooling, g_c starts to decrease below ~230 K. We conclude that there is a continuous evolution of quasistatic local fields upon cooling. At low temperatures $T \lesssim 80$ K, g_c, Δ, and the shift of the resonance fields start to saturate which implies rather temperature-independent static local fields.

The evolution of anisotropic quasi-static order and a finite quasi-static anisotropy gap well above T_C is at least a rather common feature of 2D ferromagnets. Anisotropic local fields (cf. Fig. 7) have been reported for the easy-axis vdW ferromagnets CrI_3 [48], Fe_4GeTe_2 [60], and $CrGeTe_3$ [64] as listed in Table I. In addition, a finite anisotropy gap well above T_C is also reported for CrI_3 [48]. Notably, its relative size at T_C, i.e., $\Delta(T_C)/\Delta(T = 2\,\text{K})$, is similar in Fe_3GeTe_2 and CrI_3 (see Table I). This also holds for and might be associated with the ratio of the characteristic temperatures T_Δ/T_C. Extending this comparison to the materials where quasistatic anisotropic fields have been detected above T_C suggests similar ratios T_Δ/T_C in Fe_3GeTe_2, CrI_3 [48], Fe_4GeTe_2 [60], and $CrGeTe_3$ [64].[2] The contrasting behavior $T_\Delta \simeq T_C$ has been found for $CrSiTe_3$ by Li *et al.* [63] who also reported such a coincidence for $CrGeTe_3$; for the latter experimental evidence is, however, ambiguous since the authors of Refs. [63,66] reported $T_\Delta \simeq T_C$ in contrast to those of Ref. [64] (see Table I). The examples of Fe_3GeTe_2 at hand and CrI_3, however, clearly demonstrate that in both 2D ferromagnets long-range magnetic order evolves from *anisotropic* short-range order which extends in a rather large temperature regime above T_C. At $T > T_\Delta$ isotropic short-range order is found in CrI_3 [48], which is also very likely to appear in Fe_3GeTe_2. Measurements at higher temperatures than feasible with our electron spin resonance (ESR) setup are needed to further confirm this issue.

[2]For all materials except CrI_3 and Fe_3GeTe_2 studied at hand where a finite gap is reported above T_C, T_Δ is determined from the experimental data as the onset temperature of anisotropy in the resonance fields.

TABLE II. Excitation gap in Fe_3GeTe_2 as determined by HF-FMR (this work) and as reported by previous INS studies [50,53,54].

	T_C (K)	Δ (GHz)	Δ (meV)	Ref.
$Fe_{2.92(1)}Ge_{1.02(3)}Te_2$	217	170(4)	0.70(2)	This work
$Fe_{2.86}GeTe_2$	215	230(50)[a]	0.96(20)[a]	[54]
$Fe_{2.75}GeTe_2$	150	895(50)[b]	3.7(2)[b]	[50]
$Fe_{2.72}GeTe_2$	160	~120[c]	~0.5[c]	[53]

[a]Obtained as $\Delta = 2KS$ with $K = 0.6(1)$ meV and a reduced spin $S = 0.8(1)$ as reported in Ref. [54].

[b]Note the critical discussion of this value and of the underlying data analysis in Ref. [53].

[c]While in Ref. [53] no spin gap was observed in the low-energy excitation spectra, extrapolating the Q^2-dependence of the spin waves along various directions suggests finite gap values of approximately 0.1 to 0.8 meV (24 to 192 GHz), respectively (cf. the Supplement Material of Ref. [53]).

IV. SUMMARY

We investigated the low-energy $q = 0$ magnon excitations of Fe_3GeTe_2 in external magnetic fields up to 16 T applied along the c axis and within the ab plane. At 2 K, the field dependence of the three observed magnon branches is well captured by a semiclassical domain-based model, highlighting the role of magnetic domains in the FMR response of Fe_3GeTe_2. Fitting the domain-based model to the experimental data at 2 K yields the microscopic parameters of the system: the anisotropy gap $\Delta = 170(4)$ GHz at $B = 0$ T, anisotropy field $B_A = 5.85(8)$ T and an isotropic effective g-factor $g_{ab} = g_c = 2.07(4)$, yielding an uniaxial anisotropy constant of $K = 10.50(23) \times 10^6$ erg/cm^3. At T_C, the anisotropy gap remains finite with a value of $\Delta \approx 65$ GHz, corresponding to about 38 % of its low-temperature value. The gap closes only above $T_\Delta \approx 270$ K, i.e., $T_\Delta/T_C \simeq 1.25$. Notably, the persistence of a finite anisotropy gap above T_C is accompanied by anisotropic shifts in the resonance fields, revealing the presence of anisotropic local magnetic fields above T_C. This implies anisotropic short-range magnetic order evidenced by the finite anisotropy gap and the presence of anisotropic shifts in the resonance fields. Our results show that long-range magnetic order in Fe_3GeTe_2 is driven by the magnetocrystalline anisotropy.

ACKNOWLEDGMENTS

We are grateful for valuable discussions and insightful input by A. Alfonsov. Support by Deutsche Forschungsgemeinschaft (DFG) under Germany's Excellence Strategy EXC2181/1-390900948 (The Heidelberg STRUCTURES Excellence Cluster) is gratefully acknowledged. B.G.B. acknowledges financial support from Studienförderwerk Klaus Murmann of Stiftung der Deutschen Wirtschaft with funds from BMBF (Federal Ministry of Education and Research).

DATA AVAILABILITY

The data that support the findings of this article are not publicly available. The data are available from the authors upon reasonable request.

[1] K. v. Klitzing, G. Dorda, and M. Pepper, New method for high-accuracy determination of the fine-structure constant based on quantized hall resistance, Phys. Rev. Lett. **45**, 494 (1980).

[2] K. S. Novoselov, A. K. Geim, S. V. Morozov, D. Jiang, M. I. Katsnelson, I. V. Grigorieva, S. V. Dubonos, and A. A. Firsov, Two-dimensional gas of massless dirac fermions in graphene, Nature (London) **438**, 197 (2005).

[3] Y. Ren, Z. Qiao, and Q. Niu, Topological phases in two-dimensional materials: A review, Rep. Prog. Phys. **79**, 066501 (2016).

[4] D. C. Tsui, H. L. Stormer, and A. C. Gossard, Two-dimensional magnetotransport in the extreme quantum limit, Phys. Rev. Lett. **48**, 1559 (1982).

[5] N. D. Mermin and H. Wagner, Absence of ferromagnetism or antiferromagnetism in one- or two-dimensional isotropic heisenberg models, Phys. Rev. Lett. **17**, 1133 (1966).

[6] T.-H. Han, J. S. Helton, S. Chu, D. G. Nocera, J. A. Rodriguez-Rivera, C. Broholm, and Y. S. Lee, Fractionalized excitations in the spin-liquid state of a kagome-lattice antiferromagnet, Nature (London) **492**, 406 (2012).

[7] Y. Kasahara, T. Ohnishi, Y. Mizukami, O. Tanaka, S. Ma, K. Sugii, N. Kurita, H. Tanaka, J. Nasu, Y. Motome, T. Shibauchi, and Y. Matsuda, Majorana quantization and half-integer thermal quantum Hall effect in a Kitaev spin liquid, Nature (London) **559**, 227 (2018).

[8] C. Xu, J. Feng, M. Kawamura, Y. Yamaji, Y. Nahas, S. Prokhorenko, Y. Qi, H. Xiang, and L. Bellaiche, Possible Kitaev quantum spin liquid state in 2D materials with $S = 3/2$, Phys. Rev. Lett. **124**, 087205 (2020).

[9] S. Spachmann, S. Selter, B. Büchner, S. Aswartham, and R. Klingeler, Strong uniaxial pressure dependencies evidencing spin-lattice coupling and spin fluctuations in $Cr_2Ge_2Te_6$, Phys. Rev. B **107**, 184421 (2023).

[10] S. Mondal, N. Khan, S. M. Mishra, B. Satpati, and P. Mandal, Critical behavior in the van der Waals itinerant ferromagnet Fe_4GeTe_2, Phys. Rev. B **104**, 094405 (2021).

[11] J. Arneth, K. Y. Choi, R. Kalaivanan, R. Sankar, and R. Klingeler, Signatures of a quantum critical endpoint in the Kitaev candidate $Na_2Co_2TeO_6$, Phys. Rev. B **110**, L140402 (2024).

[12] Z. Wang, T. Zhang, M. Ding, B. Dong, Y. Li, M. Chen, X. Li, J. Huang, H. Wang, X. Zhao, Y. Li, D. Li, C. Jia, L. Sun, H. Guo, Y. Ye, D. Sun, Y. Chen, T. Yang, J. Zhang *et al.*, Electric-field control of magnetism in a few-layered van der Waals ferromagnetic semiconductor, Nat. Nanotechnol. **13**, 554 (2018).

[13] K. Kim, J. Seo, E. Lee, K. T. Ko, B. S. Kim, B. G. Jang, J. M. Ok, J. Lee, Y. J. Jo, W. Kang, J. H. Shim, C. Kim, H. W. Yeom, B. Il Min, B.-J. Yang, and J. S. Kim, Large anomalous Hall current induced by topological nodal lines in a ferromagnetic van der Waals semimetal, Nat. Mater. **17**, 794 (2018).

[14] C. Gong and X. Zhang, Two-dimensional magnetic crystals and emergent heterostructure devices, Science **363**, eaav4450 (2019).

[15] K. S. Novoselov, A. Mishchenko, A. Carvalho, and A. H. Castro Neto, 2D materials and van der Waals heterostructures, Science **353**, aac9439 (2016).

[16] Y. Liu, N. O. Weiss, X. Duan, H.-C. Cheng, Y. Huang, and X. Duan, Van der Waals heterostructures and devices, Nat. Rev. Mater. **1**, 16042 (2016).

[17] L. Alahmed, B. Nepal, J. Macy, W. Zheng, B. Casas, A. Sapkota, N. Jones, A. R. Mazza, M. Brahlek, W. Jin, M. Mahjouri-Samani, S. S. L. Zhang, C. Mewes, L. Balicas, T. Mewes, and P. Li, Magnetism and spin dynamics in room-temperature van der Waals magnet Fe_5GeTe_2, 2D Mater. **8**, 045030 (2021).

[18] S. Spachmann, A. Elghandour, S. Selter, B. Büchner, S. Aswartham, and R. Klingeler, Strong effects of uniaxial pressure and short-range correlations in $Cr_2Ge_2Te_6$, Phys. Rev. Res. **4**, L022040 (2022).

[19] B. Huang, G. Clark, E. Navarro-Moratalla, D. R. Klein, R. Cheng, K. L. Seyler, D. Zhong, E. Schmidgall, M. A. McGuire, D. H. Cobden, W. Yao, D. Xiao, P. Jarillo-Herrero, and X. Xu, Layer-dependent ferromagnetism in a van der Waals crystal down to the monolayer limit, Nature (London) **546**, 270 (2017).

[20] J. Arneth, M. Jonak, S. Spachmann, M. Abdel-Hafiez, Y. O. Kvashnin, and R. Klingeler, Uniaxial pressure effects in the two-dimensional van der Waals ferromagnet CrI_3, Phys. Rev. B **105**, L060404 (2022).

[21] C. Gong, L. Li, Z. Li, H. Ji, A. Stern, Y. Xia, T. Cao, W. Bao, C. Wang, Y. Wang, Z. Q. Qiu, R. J. Cava, S. G. Louie, J. Xia, and X. Zhang, Discovery of intrinsic ferromagnetism in two-dimensional van der Waals crystals, Nature (London) **546**, 265 (2017).

[22] M. Abdel-Hafiez, G. Lingannan, A. Ali, L. Gries, R. Thiyagarajan, M. E. H. Khan, A. Abutaha, T. A. Abdel-Baset, K. Uemura, M. Mito, V. Borisov, A. Delin, R. Klingeler, M. S. R. Rao, and O. Eriksson, Pressure-tuned magnetism and band-gap modulation in layered Fe-doped $CrCl_3$, Phys. Rev. B **112**, 115145 (2025).

[23] M. A. McGuire, G. Clark, S. KC, W. M. Chance, G. E. Jellison, V. R. Cooper, X. Xu, and B. C. Sales, Magnetic behavior and spin-lattice coupling in cleavable van der Waals layered $CrCl_3$ crystals, Phys. Rev. Mater. **1**, 014001 (2017).

[24] G. Ouvrard, E. Sandre, and R. Brec, Synthesis and crystal structure of a new layered phase: The chromium hexatellurosilicate $Cr_2Si_2Te_6$, J. Solid State Chem. **73**, 27 (1988).

[25] I. Tsubokawa, On the magnetic properties of a $CrBr_3$ single crystal, J. Phys. Soc. Jpn. **15**, 1664 (1960).

[26] V. Kataev, B. Büchner, and A. Alfonsov, Electron spin resonance spectroscopy on magnetic van der Waals compounds, Appl. Magn. Reson. **55**, 923 (2024).

[27] H.-J. Deiseroth, K. Aleksandrov, C. Reiner, L. Kienle, and R. K. Kremer, Fe_3GeTe_2 and Ni_3GeTe_2–two new layered transition-metal compounds: Crystal structures, HRTEM investigations, and magnetic and electrical properties, Eur. J. Inorg. Chem. **2006**, 1561 (2006).

[28] J. Seo, D. Y. Kim, E. S. An, K. Kim, G.-Y. Kim, S.-Y. Hwang, D. W. Kim, B. G. Jang, H. Kim, G. Eom, S. Y. Seo, R. Stania, M. Muntwiler, J. Lee, K. Watanabe, T. Taniguchi, Y. J. Jo, J. Lee, B. I. Min, M. H. Jo *et al.*, Nearly room temperature ferromagnetism in a magnetic metal-rich van der Waals metal, Sci. Adv. **6**, eaay8912 (2020).

[29] A. F. May, D. Ovchinnikov, Q. Zheng, R. Hermann, S. Calder, B. Huang, Z. Fei, Y. Liu, X. Xu, and M. A. McGuire, Ferromagnetism near room temperature in the cleavable van der Waals crystal Fe_5GeTe_2, ACS Nano **13**, 4436 (2019).

[30] S. Khan, C. W. Zollitsch, D. M. Arroo, H. Cheng, I. Verzhbitskiy, A. Sud, Y. P. Feng, G. Eda, and H. Kurebayashi,

Spin dynamics study in layered van der Waals single-crystal $Cr_2Ge_2Te_6$, Phys. Rev. B **100**, 134437 (2019).

[31] Y. Zhang, H. Lu, X. Zhu, S. Tan, W. Feng, Q. Liu, W. Zhang, Q. Chen, Y. Liu, X. Luo, D. Xie, L. Luo, Z. Zhang, and X. Lai, Emergence of kondo lattice behavior in a van der Waals itinerant ferromagnet, Fe_3GeTe_2, Sci. Adv. **4**, eaao6791 (2018).

[32] B. Ding, Z. Li, G. Xu, H. Li, Z. Hou, E. Liu, X. Xi, F. Xu, Y. Yao, and W. Wang, Observation of magnetic skyrmion bubbles in a van der Waals ferromagnet Fe_3GeTe_2, Nano Lett. **20**, 868 (2020).

[33] V. Y. Verchenko, A. A. Tsirlin, A. V. Sobolev, I. A. Presniakov, and A. V. Shevelkov, Ferromagnetic order, strong magnetocrystalline anisotropy, and magnetocaloric effect in the layered telluride Fe_3-$\delta GeTe_2$, Inorg. Chem. **54**, 8598 (2015).

[34] K. Momma and F. Izumi, *VESTA3* for three-dimensional visualization of crystal, volumetric and morphology data, J. Appl. Cryst. **44**, 1272 (2011).

[35] R. K. Kremer and E. Brücher, Thermal and magnetoelastic properties of the van der Waals ferromagnet $Fe_{3-\delta}GeTe_2$: Anisotropic spontaneous magnetostriction and ferromagnetic magnon excitations, Phys. Rev. Mater. **8**, 024002 (2024).

[36] S. Liu, X. Yuan, Y. Zou, Y. Sheng, C. Huang, E. Zhang, J. Ling, Y. Liu, W. Wang, C. Zhang, J. Zou, K. Wang, and F. Xiu, Wafer-scale two-dimensional ferromagnetic Fe_3GeTe_2 thin films grown by molecular beam epitaxy, npj 2D Mater. Appl. **1**, 30 (2017).

[37] Z. Fei, B. Huang, P. Malinowski, W. Wang, T. Song, J. Sanchez, W. Yao, D. Xiao, X. Zhu, A. F. May, W. Wu, D. H. Cobden, J.-H. Chu, and X. Xu, Two-dimensional itinerant ferromagnetism in atomically thin Fe_3GeTe_2, Nat. Mater. **17**, 778 (2018).

[38] X. Hu, Y. Zhao, X. Shen, A. V. Krasheninnikov, Z. Chen, and L. Sun, Enhanced ferromagnetism and tunable magnetism in Fe_3GeTe_2 monolayer by strain engineering, ACS Appl. Mater. Interfaces **12**, 26367 (2020).

[39] A. V. Papavasileiou, M. Menelaou, K. J. Sarkar, Z. Sofer, L. Polavarapu, and S. Mourdikoudis, Ferromagnetic elements in two-dimensional materials: 2D magnets and beyond, Adv. Funct. Mater. **34**, 2309046 (2023).

[40] B. Chen, J. Yang, H. Wang, M. Imai, H. Ohta, C. Michioka, K. Yoshimura, and M. Fang, Magnetic properties of layered itinerant electron ferromagnet Fe_3GeTe_2, J. Phys. Soc. Jpn. **82**, 124711 (2013).

[41] X. Xu, Y. W. Li, S. R. Duan, S. L. Zhang, Y. J. Chen, L. Kang, A. J. Liang, C. Chen, W. Xia, Y. Xu, P. Malinowski, X. D. Xu, J. H. Chu, G. Li, Y. F. Guo, Z. K. Liu, L. X. Yang, and Y. L. Chen, Signature for non-stoner ferromagnetism in the van der Waals ferromagnet Fe_3GeTe_2, Phys. Rev. B **101**, 201104(R) (2020).

[42] L. Bischof, J. Arneth, R. Kalaivanan, R. Sankar, K.-Y. Choi, and R. Klingeler, Spin waves in $Na_2Co_2TeO_6$ studied by high-frequency/high-field ESR: Successes and failures of the triple-q model, Phys. Rev. B **112**, 104406 (2025).

[43] J. Werner, W. Hergett, M. Gertig, J. Park, C. Koo, and R. Klingeler, Anisotropy-governed competition of magnetic phases in the honeycomb quantum magnet $Na_3Ni_2SbO_6$ studied by dilatometry and high-frequency ESR, Phys. Rev. B **95**, 214414 (2017).

[44] See Supplemental Material at http://link.aps.org/supplemental/10.1103/zf74-j18j for further experimental information, magnetization and FMR data, alternative fits, and information on the the domain-based model.

[45] Z. Li, D.-H. Xu, X. Li, H.-J. Liao, X. Xi, Y.-C. Yu, and W. Wang, Abnormal critical fluctuations revealed by magnetic resonance in the two-dimensional ferromagnetic insulators, arXiv:2101.02440.

[46] J. Smit and H. Beljers, Ferromagnetic resonance absorption in $BaFe_{12}O_{19}$, a highly anisotropic crystal, Philips Res. Rep. **10**, 113 (1955).

[47] A. Aharoni, Demagnetizing factors for rectangular ferromagnetic prisms, J. Appl. Phys. **83**, 3432 (1998).

[48] M. Jonak, E. Walendy, J. Arneth, M. Abdel-Hafiez, and R. Klingeler, Low-energy magnon excitations and emerging anisotropic nature of short-range order in CrI_3, Phys. Rev. B **106**, 214412 (2022).

[49] S.-R. Kim, I. K. Park, J.-G. Yoo, J. Seo, J.-G. Kim, J.-H. Park, J. S. Kim, K. Kim, G. Lee, and K.-T. Ko, Role of orbital bond and local magnetism in Fe_3GeTe_2 and Fe_4GeTe_2: Implication for ultrathin nano devices, ACS Appl. Nano Mater. **5**, 10341 (2022).

[50] S. Calder, A. I. Kolesnikov, and A. F. May, Magnetic excitations in the quasi-two-dimensional ferromagnet $Fe_{3-x}GeTe_2$ measured with inelastic neutron scattering, Phys. Rev. B **99**, 094423 (2019).

[51] A. F. May, S. Calder, C. Cantoni, H. Cao, and M. A. McGuire, Magnetic structure and phase stability of the van der Waals bonded ferromagnet $Fe_{3-x}GeTe_2$, Phys. Rev. B **93**, 014411 (2016).

[52] M. Bander and D. L. Mills, Ferromagnetism of ultrathin films, Phys. Rev. B **38**, 12015 (1988).

[53] S. Bao, W. Wang, Y. Shangguan, Z. Cai, Z.-Y. Dong, Z. Huang, W. Si, Z. Ma, R. Kajimoto, K. Ikeuchi, S. I. Yano, S.-L. Yu, X. Wan, J.-X. Li, and J. Wen, Neutron spectroscopy evidence on the dual nature of magnetic excitations in a van der Waals metallic ferromagnet $Fe_{2.72}GeTe_2$, Phys. Rev. X **12**, 011022 (2022).

[54] C. Trainer, O. R. Armitage, H. Lane, L. C. Rhodes, E. Chan, I. Benedičič, J. A. Rodriguez-Rivera, O. Fabelo, C. Stock, and P. Wahl, Relating spin-polarized STM imaging and inelastic neutron scattering in the van der Waals ferromagnet Fe_3GeTe_2, Phys. Rev. B **106**, L081405 (2022).

[55] Q. Li, M. Yang, C. Gong, R. V. Chopdekar, A. T. N'Diaye, J. Turner, G. Chen, A. Scholl, P. Shafer, E. Arenholz, A. K. Schmid, S. Wang, K. Liu, N. Gao, A. S. Admasu, S.-W. Cheong, C. Hwang, J. Li, F. Wang, X. Zhang *et al.*, Patterning-induced ferromagnetism of Fe_3GeTe_2 van der Waals materials beyond room temperature, Nano Lett. **18**, 5974 (2018).

[56] N. León-Brito, E. D. Bauer, F. Ronning, J. D. Thompson, and R. Movshovich, Magnetic microstructure and magnetic properties of uniaxial itinerant ferromagnet Fe_3GeTe_2, J. Appl. Phys. **120**, 083903 (2016).

[57] G. D. Nguyen, J. Lee, T. Berlijn, Q. Zou, S. M. Hus, J. Park, Z. Gai, C. Lee, and A.-P. Li, Visualization and manipulation of magnetic domains in the quasi-two-dimensional material Fe_3GeTe_2, Phys. Rev. B **97**, 014425 (2018).

[58] H.-H. Yang, N. Bansal, P. Rüßmann, M. Hoffmann, L. Zhang, D. Go, Q. Li, A.-A. Haghighirad, K. Sen, S. Blügel, M. Le Tacon, Y. Mokrousov, and W. Wulfhekel, Magnetic domain walls of the van der Waals material Fe_3GeTe_2, 2D Mater. **9**, 025022 (2022).

[59] J. Yi, H. Zhuang, Q. Zou, Z. Wu, G. Cao, S. Tang, S. A. Calder, P. R. C. Kent, D. Mandrus, and Z. Gai, Competing antiferromagnetism in a quasi-2D itinerant ferromagnet: Fe_3GeTe_2, 2D Mater. **4**, 011005 (2017).

[60] R. Pal, J. J. Abraham, A. Mistonov, S. Mishra, N. Stilkerich, S. Mondal, P. Mandal, A. N. Pal, J. Geck, B. Büchner, V. Kataev, and A. Alfonsov, Disentangling the unusual magnetic anisotropy of the near-room-temperature ferromagnet Fe_4GeTe_2, Adv. Funct. Mater. **34**, 2402551 (2024).

[61] X. Shen, H. Chen, Y. Li, H. Xia, F. Zeng, J. Xu, H. Y. Kwon, Y. Ji, C. Won, W. Zhang, and Y. Wu, Multi-domain ferromagnetic resonance in magnetic van der Waals crystals CrI_3 and $CrBr_3$, J. Magn. Magn. Mater. **528**, 167772 (2021).

[62] J. F. Dillon, Jr. and C. E. Olson, Magnetization, resonance, and optical properties of the ferromagnet CrI_3, J. Appl. Phys. **36**, 1259 (1965).

[63] Z. Li, D.-H. Xu, X. Li, H.-J. Liao, X. Xi, Y.-C. Yu, and W. Wang, Anomalous spin dynamics in a two-dimensional magnet induced by anisotropic critical fluctuations, Phys. Rev. B **106**, 054427 (2022).

[64] J. Zeisner, A. Alfonsov, S. Selter, S. Aswartham, M. P. Ghimire, M. Richter, J. van den Brink, B. Büchner, and V. Kataev, Magnetic anisotropy and spin-polarized two-dimensional electron gas in the van der Waals ferromagnet $Cr_2Ge_2Te_6$, Phys. Rev. B **99**, 165109 (2019).

[65] X. Zhang, Y. Zhao, Q. Song, S. Jia, J. Shi, and W. Han, Magnetic anisotropy of the single-crystalline ferromagnetic insulator $Cr_2Ge_2Te_6$, Jpn. J. Appl. Phys. **55**, 033001 (2016).

[66] Y. Wang, Q. Fu, S. Ji, X. Yin, Y. Chen, R. Liu, and X. Li, Temperature-dependent magnetic order of two-dimensional ferromagnetic $Cr_2Ge_2Te_6$ single crystal, J. Alloys Compd. **931**, 167401 (2023).

[67] V. Carteaux, D. Brunet, G. Ouvrard, and G. Andre, Crystallographic, magnetic and electronic structures of a new layered ferromagnetic compound $Cr_2Ge_2Te_6$, J. Phys.: Condens. Matter **7**, 69 (1995).